Supplementary Information for "Strong coupling between a single-photon and a two-photon Fock state"

Shuai-Peng Wang,[1,2,3] Alberto Mercurio,[4,5] Alessandro Ridolfo,[6] Yuqing Wang,[1] Mo Chen,[1] Wenyan Wang,[1] Yulong Liu,[1] Huanying Sun,[1] Tiefu Li,[7,1,*] Franco Nori,[8,9] Salvatore Savasta,[10,†] and J. Q. You[3,‡]

[1] *Beijing Academy of Quantum Information Sciences, Beijing 100193, China*
[2] *Quantum Physics and Quantum Information Division, Beijing Computational Science Research Center, Beijing 100193, China*
[3] *Zhejiang Key Laboratory of Micro-Nano Quantum Chips and Quantum Control, School of Physics, and State Key Laboratory for Extreme Photonics and Instrumentation, Zhejiang University, Hangzhou 310027, China*
[4] *Institute of Physics, École Polytechnique Fédérale de Lausanne (EPFL), CH-1015 Lausanne, Switzerland*
[5] *Center for Quantum Science and Engineering, École Polytechnique Fédérale de Lausanne (EPFL), CH-1015 Lausanne, Switzerland*
[6] *Dipartimento di Fisica e Astronomia, Università di Catania, 95123 Catania, Italy*
[7] *School of Integrated Circuits, and Frontier Science Center for Quantum Information, Tsinghua University, Beijing 100084, China*
[8] *Quantum Computing Center, RIKEN, Wako-shi, Saitama 351-0198, Japan*
[9] *Physics Department, The University of Michigan, Ann Arbor, Michigan 48109-1040, USA*
[10] *Dipartimento di Scienze Matematiche e Informatiche, Scienze Fisiche e Scienze della Terra, Università di Messina, I-98166 Messina, Italy*

EXPERIMENTAL SETUP

The experimental setup is shown in Supplementary Fig. 1. The transmission spectra of the multimode ultrastrongly-coupled qubit–resonator system in Fig. 2 of the main text are measured with a vector network analyzer. A signal generator and a spectrum analyzer are used for the SHG and the interference measurements in Fig. 3 and Fig. 4 of the main text.

A current source is used to generate the external flux bias $\delta\Phi_{\rm ext}$ via an on-chip control line. The input signals are all attenuated and filtered at different temperature stages in the dilution refrigerator before reaching the sample. The output signals are amplified by both a cryogenic and a room temperature amplifier before being collected by the network analyzer and the spectrum analyzer. Isolators and low-pass filters (LPF) are used to protect the sample from the amplifiers' noise.

The data presented in Figs. 2, 3, and 4 in the main text were all acquired as coherent signals using a vector network analyzer (VNA). For Fig. 2 in the main text, the VNA was employed to measure the S21 parameter of the transmitted signal. In the case of Fig. 3 in the main text, the VNA detected the SHG signal emanating from the device, which was excited by an external signal generator. The VNAs output port was terminated, and it functioned solely to capture the SHG signal. For Fig. 4 in the main text, the VNA measured the S21 parameter of the signal at the frequency $\omega/2\omega$, while a simultaneous signal at $2\omega/\omega$ frequency was applied from a separate signal generator.

THEORY

Circuit quantization

To derive the total Hamiltonian of the system, here we follow the procedure applied in Ref. [1], where the quantization was applied to the case of a single Josephson junction or a superconducting quantum interference device (SQUID) embedded in a transmission line, while here we consider the flux qubit. A similar procedure can also be found in Ref. [2]. The flux qubit circuit is composed by a loop of three Josephson junctions, as in Supplementary Fig. 1. Without the qubit, the Lagrangian of the bare transmission line is given by [3]

$$\mathcal{L}_{\rm tl}=\int_{-l}^{l}\left[\frac{c_0}{2}\dot{\psi}^2(x,t)-\frac{[\partial_x\psi(x,t)]^2}{2l_0}\right]dx\,, \tag{1}$$

where c_0 and l_0 are the capacitance and inductance per unit length, respectively, and $\psi(x,t)$ is the flux along the waveguide. For simplicity, we consider c_0 and l_0 as constants, although the inhomogeneous geometry of the waveguide in the region of the qubit can make them space-dependent [4]. The qubit is placed at the point x_0, and the related Lagrangian is

$$\begin{aligned}\mathcal{L}_{\rm q}=&\frac{C_j}{2}\dot{\varphi}^2+\frac{C_j}{2}\dot{\varphi_1}^2+\frac{\alpha C_j}{2}\dot{\varphi_2}^2\\&+E_j\cos\left(\frac{\varphi}{\varphi_0}\right)+E_j\cos\left(\frac{\varphi_1}{\varphi_0}\right)\\&+\alpha E_j\cos\left(\frac{\varphi_2}{\varphi_0}\right),\end{aligned} \tag{2}$$

where C_j and E_j are the capacitance and energy of the junction, $\varphi_0=\hbar/(2e)$ is the reduced flux quantum, φ_1 and φ_2 are the fluxes across the junctions in the lower

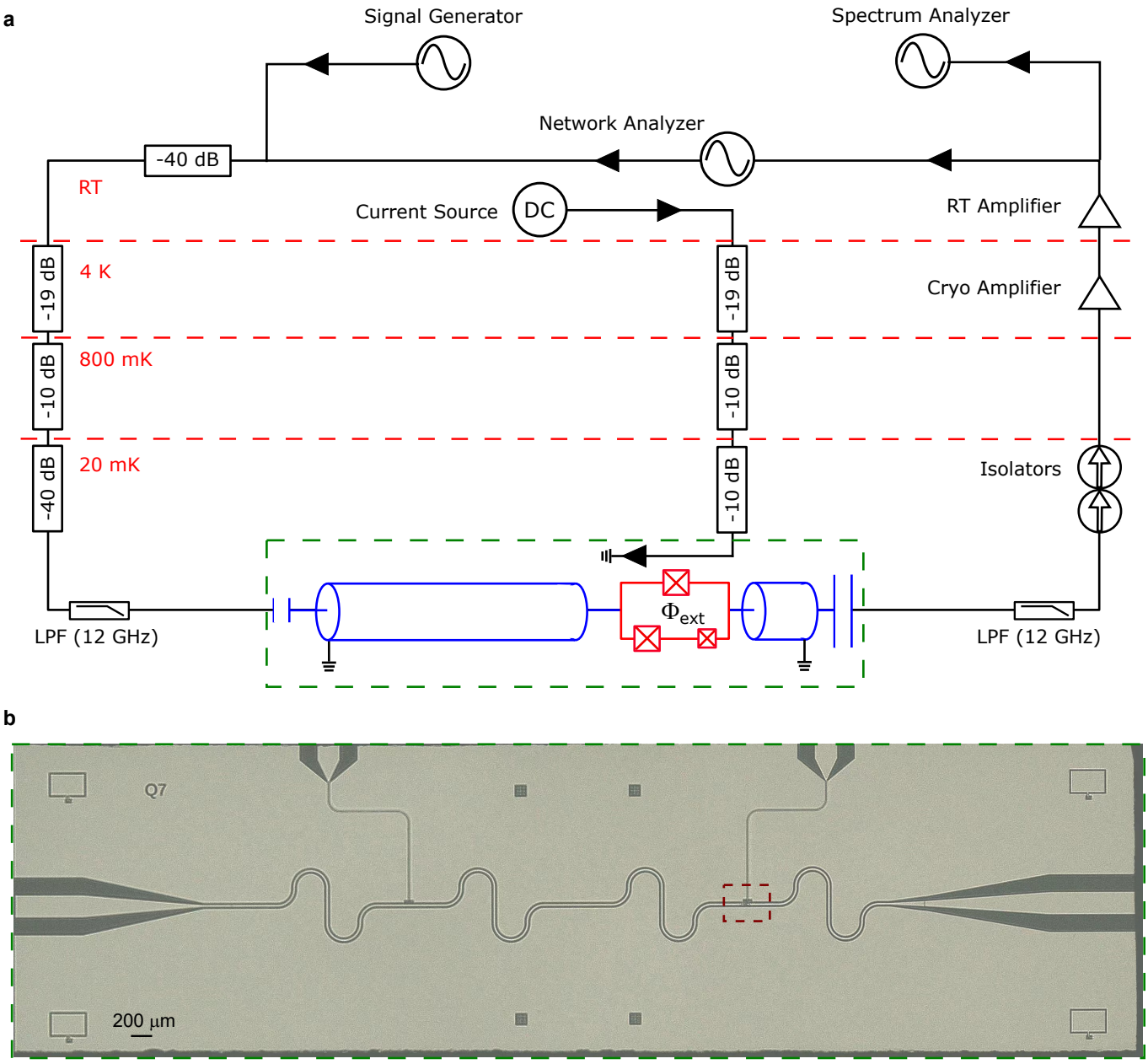

Supplementary Fig. 1. **a,** Schematic of the experimental setup. RT: room temperature. Cryo: cryogenic. LPF: low pass filter. The green dashed rectangle indicates the region of the chip. **b,** The optical image of the chip. The red dashed rectangle indicates the location of the flux qubit.

arm, while $\varphi = \psi(x_0^+, t) - \psi(x_0^-, t)$ is the flux across the junction in the upper arm.

By moving the quadratic term of $\cos(\varphi/\varphi_0)$ into the resonator term, the total Lagrangian can be expressed as

$$\mathcal{L} = \mathcal{L}'_{\rm tl} + \mathcal{L}'_{\rm q}\,, \tag{3}$$

where the prime in the resonator term indicates that it includes the quadratic term $E_j\varphi^2/(2\varphi_0^2)$, while the prime in the qubit term indicates that it does not include this term.

To proceed with the quantization, we need to express the resonator Lagrangian in terms of the normal modes. This can be done by solving the Euler-Lagrange equation

$$\sum_{\nu=x,t} \partial_\nu \left(\frac{\partial \mathcal{L}'_{\rm tl}}{\partial\left[\partial_\nu \psi(x,t)\right]} \right) - \frac{\partial \mathcal{L}'_{\rm tl}}{\partial \psi(x,t)} = 0\,, \tag{4}$$

together with the boundary conditions at the two ends of the resonator and the constraint dictated by the qubit at position x_0. We now express the field in terms of the modes

$$\psi(x,t) = \sum_n \psi_n(t) u_n(x)\,, \tag{5}$$

with $\ddot{\psi}_n(t) = -\omega_n^2\psi_n(t)$ a function of time oscillating at mode frequency ω_n and $u_n(x)$ are determined by the boundary conditions. We define these functions to be of the form

$$u_n(x) = A_n \begin{cases} \sin\left[k_n\left(x+l\right)-\phi_n\right] & \text{for } -l \le x < x_0^- \,, \\ B_n \sin\left[k_n\left(x-l\right)+\phi_n\right] & \text{for } x_0^+ < x \le l \,, \end{cases} \tag{6}$$

with $k_n = \omega_n\sqrt{l_0 c_0}$, A_n, B_n and ϕ_n are constants determined by the various constraints. The boundary conditions at the two ends of the resonator are

$$\frac{1}{l_0}\frac{\partial\psi(x,t)}{\partial x}\bigg|_{x=-l,l} = 0 \,, \tag{7}$$

which imply $\phi_n = \pi/2$. The current on both sides of the qubit is equal, giving the condition

$$\frac{1}{l_0}\frac{\partial\psi(x,t)}{\partial x}\bigg|_{x=x_0^-} = \frac{1}{l_0}\frac{\partial\psi(x,t)}{\partial x}\bigg|_{x=x_0^+} = C_j\ddot{\varphi} + \frac{\varphi}{L_j} \,, \tag{8}$$

with $L_j = \varphi_0^2/E_j$ the flux-dependent Josephson inductance. The first equation gives the value of B_n

$$B_n = \frac{\cos\left[k_n\left(x_0+l\right)-\phi_n\right]}{\cos\left[k_n\left(x_0-l\right)+\phi_n\right]} \,. \tag{9}$$

The value of k_n is found by inserting the mode shape in Supplementary Eq. (6) into the constraint in Supplementary Eq. (8), giving the following transcendental equation

$$\begin{aligned} &\left\{\tan\left[k_n\left(x_0-l\right)+\phi_n\right] - \tan\left[k_n\left(x_0+l\right)-\phi_n\right]\right\} \\ &\times\left[\frac{l_0 l}{L_j} - \left(k_n l\right)^2\frac{C_j}{c_0 l}\right] - k_n l = 0 \,. \end{aligned} \tag{10}$$

The profile shapes $u_n(x)$ satisfy the orthonormality condition [1]

$$\langle u_n(x)\cdot u_m(x)\rangle = C_\Sigma\delta_{nm} \,, \tag{11}$$

with $C_\Sigma = 2lc_0 + C_j$.

Using the orthonormality condition above and the mode decomposition in Supplementary Eq. (6), we can express the total Lagrangian in terms of the normal modes

$$\mathcal{L} = \sum_n\left(\frac{C_\Sigma}{2}\dot{\psi}_n^2 - \frac{\psi_n^2}{2L_n}\right) + \mathcal{L}_\mathrm{q} \,, \tag{12}$$

with $L_n = \omega_n^2 C_\Sigma$.

When applying an external field Φ_ext, the three junction fluxes are related by the flux quantization

$$\varphi + \varphi_1 + \varphi_2 = \Phi_\mathrm{ext} \,. \tag{13}$$

Thus, we can express φ_2 in terms of φ, φ_1 and Φ_ext. We now pass to the Hamiltonian formalism, obtaining

$$\begin{aligned} H = &\sum_n\left(\frac{q_n^2}{2C_\Sigma} + \frac{\psi_n^2}{2L_n}\right) + \frac{\varphi^2}{2L_j} + \frac{q_1^2}{2C_j} \\ &- E_j\cos\left(\frac{\varphi}{\varphi_0}\right) - E_j\cos\left(\frac{\varphi_1}{\varphi_0}\right) \\ &- \alpha E_j\cos\left(\frac{\Phi_\mathrm{ext}-\varphi-\varphi_1}{\varphi_0}\right) \,, \end{aligned} \tag{14}$$

where $\varphi = \sum_n \psi_n\Delta u_n$ is a resonator variable, with $\Delta u_n = u_n(x_0^+) - u_n(x_0^-)$.

By using the trigonometric property $\cos(x+y) = \cos x\cos y - \sin x\sin y$ and the last term, with $x = (\varphi-\Phi_\mathrm{ext})/\varphi_0$ and $y = \varphi_1/\varphi_0$, we can express the Hamiltonian in the form

$$\begin{aligned} H = &\sum_n\left(\frac{q_n^2}{2C_\Sigma} + \frac{\psi_n^2}{2L_n}\right) + \frac{\varphi^2}{2L_j} + \frac{q_1^2}{2C_j} \\ &- \tilde{E}_j(\Phi_\mathrm{ext})\cos\left(\frac{\varphi}{\varphi_0}-\delta_0\right) - E_j\cos\left(\frac{\varphi_1}{\varphi_0}\right) \\ &- \alpha E_j\cos\left(\frac{\varphi-\Phi_\mathrm{ext}}{\varphi_0}\right)\left[\cos\left(\frac{\varphi_1}{\varphi_0}\right)-1\right] \\ &+ \alpha E_j\sin\left(\frac{\varphi-\Phi_\mathrm{ext}}{\varphi_0}\right)\sin\left(\frac{\varphi_1}{\varphi_0}\right) \,, \end{aligned} \tag{15}$$

where

$$\tilde{E}_j(\Phi_\mathrm{ext}) = E_j\sqrt{1+\alpha^2\tan^2\left(\frac{\Phi_\mathrm{ext}}{2\varphi_0}\right)}\cos\left(\frac{\Phi_\mathrm{ext}}{2\varphi_0}\right) \tag{16}$$

is the flux-dependent Josephson energy, and $\delta_0 = \alpha\tan(\Phi_\mathrm{ext}/2\varphi_0)$ is the phase shift. By expanding the term $\tilde{E}_j(\Phi_\mathrm{ext})\cos\left(\frac{\varphi}{\varphi_0}-\delta_0\right)$ up to the second order, we obtain a flux-dependent renormalization of the bare modes frequencies $\omega_n'(\Phi_\mathrm{ext})$, together with a flux-dependent self- and cross-Kerr [1]. Here we neglect the effect of the Kerr terms, as they don't play a significant role in the dynamics studied in this work, while the renormalization of the frequency of the modes gives the V-shape behavior. A similar flux-dependent renormalization of the modes frequencies is also present in a flux qubit interacting with a LC resonator [5].

We now quantize the Hamiltonian in Supplementary Eq. (15). Furthermore, we can apply the trigonometric property to separate the terms in $\varphi-\Phi_\mathrm{ext}$ in the last two terms, and then expanding them up to first order in φ, obtaining the following Hamiltonian

$$\begin{aligned} H \simeq &\sum_n\hbar\omega_n'(\Phi_\mathrm{ext})a_n^\dagger a_n + \frac{q_1^2}{2C_j} - E_j\cos\left(\frac{\varphi_1}{\varphi_0}\right) \\ &- \alpha E_j\cos\left(\frac{\Phi_\mathrm{ext}}{\varphi_0}\right)\left[\cos\left(\frac{\varphi_1}{\varphi_0}\right)-1\right] \\ &- \alpha E_j\sin\left(\frac{\Phi_\mathrm{ext}}{\varphi_0}\right)\sin\left(\frac{\varphi_1}{\varphi_0}\right) \\ &+ \frac{\alpha E_j}{\varphi_0^2}\cos\left(\frac{\Phi_\mathrm{ext}}{\varphi_0}\right)\varphi\varphi_1 \,. \end{aligned} \tag{17}$$

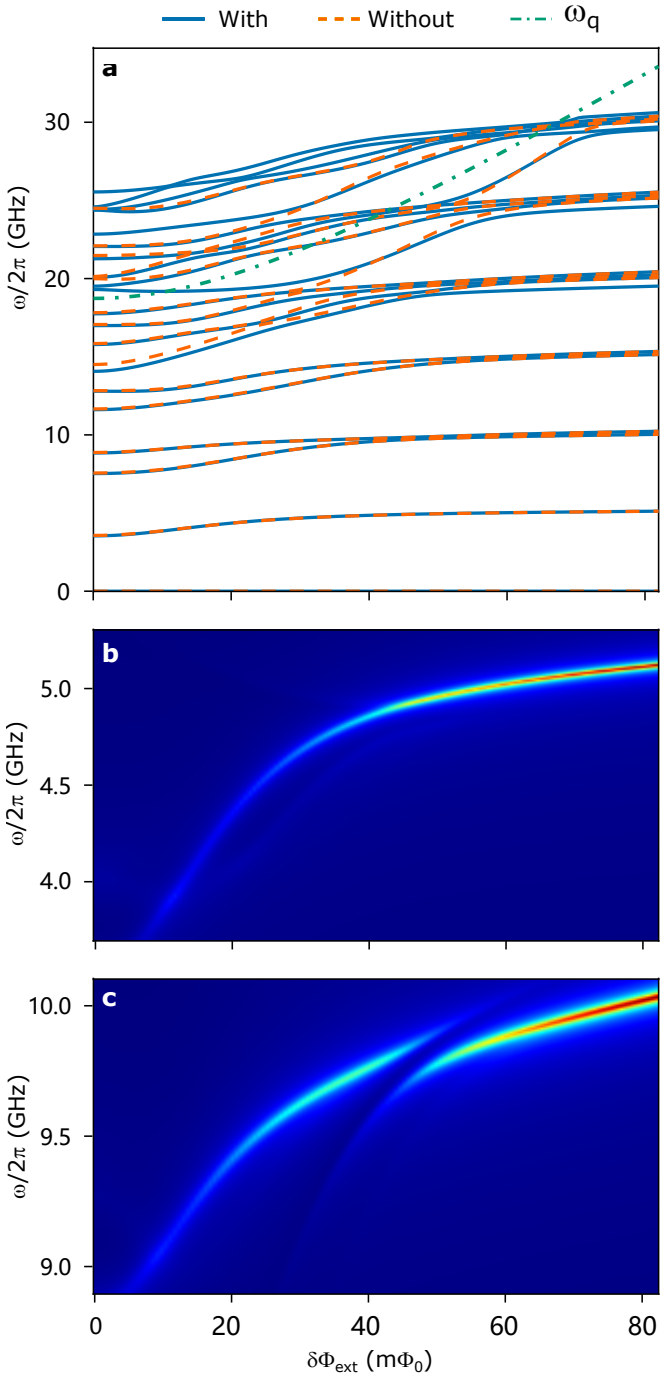

Supplementary Fig. 2. Influence of the fourth mode of the resonator. **a,** eigenvalues of the total Hamiltonian (solid blue) including the fourth mode with coupling $g_4/2\pi = 2$ GHz, without the fourth mode (dashed orange) and bare qubit frequency (dash-dotted green) as a function of the flux bias $\delta\Phi_{\rm ext}$. The qubit becomes resonant with the fourth mode at $\delta\Phi_{\rm ext} \simeq 40$ mΦ_0. However, the low energy eigenvalues remain unperturbed. **b, c** transmission spectra for the first and second mode, respectively. The results are indentical to the ones presented in the main text.

Notice that we have neglected the term $\varphi[\cos(\varphi_1/\varphi_0)-1]$ and considered $\varphi\sin(\varphi_1/\varphi_0) \simeq \varphi\varphi_1/\varphi_0$. Not doing these approximations would only lead to a small renormalization of the coupling strengths and modes frequencies, when projecting in the two-level subspace.

By projecting the total Hamiltonian into the two lowest-energy levels of the qubit, we get

$$H = \frac{\hbar\omega_q}{2}\sigma_z + \sum_n \left[\hbar\omega_n'(\Phi_{\rm ext})a_n^\dagger a_n + \hbar g_n\left(-\sin\theta\,\sigma_x + \cos\theta\,\sigma_z\right)\left(a_n + a_n^\dagger\right)\right], \tag{18}$$

with

$$g_n = \cos\left(\frac{\Phi_{\rm ext}}{\varphi_0}\right)\frac{\alpha E_j}{\hbar\varphi_0}\sqrt{\frac{\hbar}{2C_\Sigma\omega_n}}\Delta u_n\,, \tag{19}$$

which is equivalent to the Hamiltonian in Eq. (1) of the main text, but expressed in the qubit energy basis instead of the persistent current one. The qubit position corresponds to the current node of the third mode of the waveguide ($\Delta u_3 \approx 0$), leading to $g_3 \approx 0$. Hence, we can consider only the first and second modes for the energy region we studied here. Numerical calculation using circuit design parameters (i.e., $l_0 = 0.43$ nH/mm, $c_0 = 0.16$ pF/mm, $L_j \approx 0.94$ nH, $C_j \approx 11$ fF, $l = 4.7$ mm) shows that $g_1/2\pi \approx 2.53$ GHz and $g_2/2\pi \approx 2.70$ GHz near the optimal point ($\Phi_{\rm ext}/\varphi_0 \simeq \pi$), which qualitatively agree with the fitted values in the main text. A study of the influence of the fourth mode is presented in the next section.

Influence of higher modes

Although the physics of this work involves only the first two modes of the waveguide resonator, here we study the influence of the higher energy modes. The position of the qubit coincides with the node of the third mode, corresponding to a negligible coupling. Hence, we now study the influence of the fourth mode on both the eigenvalues and the transmission spectrum.

Supplementary Fig. 2a shows the first eigenvalues of the total Hamiltonian with and without the fourth mode (solid blue and dashed orange lines, respectively), together with the bare qubit frequency (dash-dotted green line). Although the qubit is in resonance with the fourth mode at approximately $\delta\Phi_{\rm ext} \simeq 40$ mΦ_0, the eigenvalues in the low energy region remain unperturbed. In Supplementary Fig. 2b,c we show that also the transmission spectra are unaltered by the presence of the fourth mode. Again, the spectra is obtained using a low power input drive, involving less then one photon. This keeps the dynamics inside the low-energy subspace.

Efficiency of the Second Harmonic Generation

Here we define the efficiency

$$\eta \equiv S_{21}^{(2\omega)}/S_{21}^{(\omega)} \tag{20}$$

of the SHG as the ratio between the signal transmitted at 2ω over the one at ω, when driving at ω. This quantity gives us more information on the number of photons up-converted per unit incoming photon. Supplementary Fig. 3 shows the SHG efficiency as a function of the theoretical input photon number $\bar{n}_1$. This value is significant already for very small number of input photons.

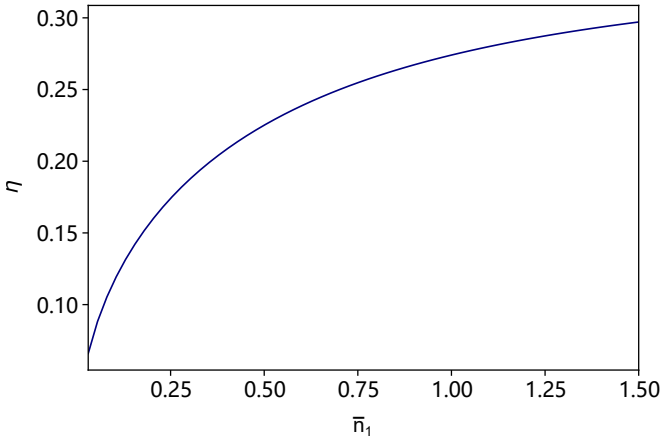

Supplementary Fig. 3. Theoretically calculated efficiency of the second harmonic generation as a function of the theoretical input photon number $\bar{n}_1$. This quantity is related to the number of photons emitted at frequency 2ω per unit input photon at ω. This simulation was performed at $\delta\Phi_{\rm ext} = -45\ {\rm m}\Phi_0$.

Input–output and generalized master equation

We start by considering the losses of the two-mode resonator field due to the presence of both the input and output ports, where the resonator is capacitively coupled to open coplanar waveguides. On the input side, the interaction term can be described as

$$\mathcal{V}_l = i\int_0^\infty {\rm d}\omega\, g_l(\omega)\left(a_{l,\omega} - a_{l,\omega}^\dagger\right) X\,, \tag{21}$$

where $g_l(\omega) = \sqrt{\kappa_l\omega/\omega_1}$ is the frequency dependent bath–resonator coupling rate (expressed in terms of the bare loss rate κ_l), and

$$X = i(a_1 - a_1^\dagger) + i\sqrt{\frac{\omega_2}{\omega_1}}(a_2 - a_2^\dagger) \tag{22}$$

is the adimensional two-mode field momentum. Assuming the driving tone at frequency $\omega_{\rm in}$ to be in a coherent state, the input creation operator $|\alpha_{\rm in}\rangle$ can be decomposed into the sum of a zero-mean quantum operator $\tilde{a}_{l,\omega}$ plus a c-number: $a_{l,\omega} = \tilde{a}_{l,\omega} + \delta(\omega-\omega_{\rm in})\alpha_{\rm in}\exp(i\omega_{\rm in}t)$. Using $\alpha_{\rm in} = |\alpha_{\rm in}|\exp\{i\phi\}$, the resulting driving term is

$$\mathcal{V}_{\rm in}(t) = 2|\alpha_{\rm in}|\sqrt{\kappa_l}\sqrt{\frac{\omega_{\rm in}}{\omega_1}}\sin(\omega_{\rm in}t+\phi)X\,. \tag{23}$$

Here $|\alpha_{\rm in}|^2$ describes the rate of input photons and can be directly related to the input power: $P_{\rm in} = \hbar\omega_{\rm in}|\alpha_{\rm in}|^2$. Supplementary Eq. (23) can be easily generalized to two (or more) driving tones. When considering a single tone, $\alpha_{\rm in}$ can be assumed to be real without any loss of generality. However, in the multi-tone case, the relative phase between different tones becomes relevant (see, e.g., Fig. 4 in the main text). On the output side, we have an analogous term

$$\mathcal{V}_r = i\int_0^\infty {\rm d}\omega\, g_r(\omega)\left(a_{{\rm r},\omega} - a_{{\rm r},\omega}^\dagger\right) X\,, \tag{24}$$

with $g_r(\omega) = \sqrt{\kappa_r\omega/\omega_1}$. In the Heisenberg picture, we define the positive frequency part of the output field operator [6] as

$$\Phi^+_{\rm r,out}(t) = \frac{1}{\sqrt{2\pi}}\int_0^\infty {\rm d}\omega\,\frac{1}{\sqrt{\omega}}e^{-i\omega(t-t_f)}a_{{\rm r},\omega}(t_f)\,, \tag{25}$$

where t_f is the time at which the measurement is performed, and we assume that there is no input field from the output port $\langle\Phi^+_{\rm r,in}(t)\rangle = 0$.

We now take the positive frequency part of the system field operator

$$X^+ \equiv \sum_{j>k} X_{kj} \tag{26}$$

($X_{kj} \equiv X_{kj}\,|k\rangle\langle j|$), which is written in the basis of the eigenstates of the system Hamiltonian, with $|j\rangle$ being the j-th eigenstate and $X_{kj} = \langle k|X|j\rangle$. By performing the rotating-wave approximation in Supplementary Eq. (24)

$$\left(a_{{\rm r},\omega} - a_{{\rm r},\omega}^\dagger\right)X \simeq a_{{\rm r},\omega}X^- - a_{{\rm r},\omega}^\dagger X^+\,, \tag{27}$$

and following the standard input–output procedure [6], the relation between $\Phi^+_{\rm out}$ and X^+ is

$$\left\langle\Phi^+_{\rm r,out}\right\rangle(t) = \sqrt{\frac{\kappa_{\rm r}}{\omega_1}}\left\langle X^+\right\rangle(t)\,, \tag{28}$$

where the time dependence of $\langle X^+\rangle(t)$ originates from the Hamiltonian dynamics, dissipations, and the coherent input field $\mathcal{V}_{\rm in}(t)$. Moreover, it is often useful to write the input–output relation in terms of $\dot{\Phi}^+_{\rm r,out}$ rather than $\Phi^+_{\rm r,out}$, because it is directly linked to the measurement of the voltage.

Compared to the standard treatment of driven-dissipative systems, the explicit time dependence cannot be traced out through a unitary transformation, due to the presence of the counter-rotating terms. This results in a time-dependent stroboscopic steady state $\rho_{\rm ss}(t)$ for $t\to\infty$, which, following the Floquet formalism, is periodic, with period $T = 2\pi/\omega_{\rm in}$. Indeed, the time evolution of the total density matrix follows the generalized master equation $\dot{\rho} = \mathcal{L}_{\rm gme}(t)\rho$, where

$$\mathcal{L}_{\rm gme}(t) = \mathcal{L}_0 + \mathcal{L}_1\exp(i\omega_{\rm in}t) + \mathcal{L}_{-1}\exp(-i\omega_{\rm in}t)\,. \tag{29}$$

Here $\mathcal{L}_0$ describes the open evolution of the system in the absence of any external drive, taking into account

losses of the resonator in both the input and output ports and possible additional internal loss. It also takes into account intrinsic qubit loss and pure dephasing with rates κ_q and $\kappa_{q,\mathrm{dep}}$, respectively. Indeed, the Liouvillian can be written as [7]

$$\begin{aligned}\mathcal{L}_0\rho = &-i[H_S,\rho] + \frac{1}{2}\sum_{\substack{n=(r_1,r_2,q)\\ j,k>j\\ l,m>l}} \tilde{\kappa}^{(n)}(\tilde{\omega}_{ml})\times \\ &\Big\{ \Big[X^{(n)\dagger}_{lm}\rho X^{(n)}_{jk} - X^{(n)}_{jk}X^{(n)\dagger}_{lm}\rho\Big]\, n_{\mathrm{th}}(\tilde{\omega}_{ml},T_n) \\ &+ \Big[X^{(n)}_{lm}\rho X^{(n)\dagger}_{jk} - X^{(n)\dagger}_{jk}X^{(n)}_{lm}\rho\Big]\, [n_{\mathrm{th}}(\tilde{\omega}_{ml},T_n)+1] \\ &+ \Big[X^{(n)\dagger}_{jk}\rho X^{(n)}_{lm} - \rho X^{(n)}_{lm}X^{(n)\dagger}_{jk}\Big]\, n_{\mathrm{th}}(\tilde{\omega}_{ml},T_n) \\ &+ \Big[X^{(n)}_{jk}\rho X^{(n)\dagger}_{lm} - \rho X^{(n)\dagger}_{lm}X^{(n)}_{jk}\Big]\, [n_{\mathrm{th}}(\tilde{\omega}_{ml},T_n)+1]\Big\} \\ &+ \kappa_{q,\mathrm{dep}}\mathcal{D}\Big[\sum_j X^{(q)}_{jj}\Big]\rho\,,\end{aligned} \tag{30}$$

where

$$X^{(r_1)} = i(a_1 - a_1^\dagger) + i\sqrt{\frac{\omega_2}{\omega_1}}(a_2 - a_2^\dagger)\,, \tag{31a}$$

$$X^{(r_2)} = \sqrt{\frac{\omega_2}{\omega_1}}(a_1 + a_1^\dagger) + (a_2 + a_2^\dagger)\,, \tag{31b}$$

$$X^{(q)} = \sigma_z \tag{31c}$$

are the dissipation operators, and $\tilde{\omega}_{ml} = \tilde{\omega}_m - \tilde{\omega}_l$. Here $X^{(r_1)}$ is related to the dissipation induced by the interaction with the coplanar waveguide, $X^{(r_2)}$ is related to the internal loss through the inductance, and $X^{(q)}$ is related to the qubit dissipation. Moreover,

$$\tilde{\kappa}^{(r_1)}(\omega) = (\kappa_l + \kappa_r)\omega/\omega_1\,, \tag{32a}$$

$$\tilde{\kappa}^{(r_2)}(\omega) = \kappa_{\mathrm{int}}\omega/\omega_1\,, \tag{32b}$$

$$\tilde{\kappa}^{(q)}(\omega) = \kappa_q\omega/\omega_1\,, \tag{32c}$$

and

$$n_{\mathrm{th}}(\omega,T_n) = [\exp(\hbar\omega/k_{\mathrm{B}}T_n) - 1]^{-1} \tag{33}$$

is the thermal population of the n-th reservoir describing the number of excitations at a given temperature T_n; k_{B} is the Boltzmann constant, and

$$\mathcal{D}[O]\,\rho = \frac{1}{2}\left(2O\rho O^\dagger - O^\dagger O\rho - \rho O^\dagger O\right) \tag{34}$$

is the standard Lindblad dissipator. This term considers qubit pure dephasing effects due to stochastic fluctuations of the flux passing through the qubit, inducing additional decoherence effects.

It is worth to introduce real loss rates (directly related to the decay rate of a specific transition, corresponding to their spectral linewidths). For a given transition $\tilde{\omega}_{p,q}$ [which corresponds to the case where $(l,m) = (j,k) = (q,p)$ in Supplementary Eq. (30)], the total loss rate is then

$$\Gamma_{p,q} = \tilde{\kappa}^{(r_1)}(\tilde{\omega}_{p,q})|X^{(r_1)}_{pq}|^2 + \tilde{\kappa}^{(r_2)}(\tilde{\omega}_{p,q})|X^{(r_2)}_{p,q}|^2\,, \tag{35}$$

where we considered here only the resonator losses. Note that the relevant transitions studied here are not significantly affected by qubit decoherence. As an example, the linewidth of the transition at $\tilde{\omega}_1$ is

$$\Gamma_{1,0} = (\kappa_{\mathrm{in}} + \kappa_{\mathrm{out}})|X^{(r_1)}_{10}|^2 + \kappa_{\mathrm{int}}|X^{(r_2)}_{10}|^2\,. \tag{36}$$

The influence of the coherent input drive comes from $\mathcal{L}_\pm$, where

$$\mathcal{L}_{\pm1}\rho = \pm i|\alpha_{\mathrm{in}}|e^{\pm i\phi}\sqrt{\kappa_{\mathrm{in}}}\sqrt{\frac{\omega_{\mathrm{in}}}{\omega_1}}[X,\rho]\,. \tag{37}$$

Following Supplementary Eq. (29), we can expand the steady state in Fourier components $\rho_{\mathrm{ss}}(t) = \sum_{n=-\infty}^{+\infty}\rho_n\exp(in\omega_{\mathrm{in}}t)$. By putting this form of the density matrix into Supplementary Eq. (29), and equating each Fourier component, we obtain a tridiagonal recursion relation

$$(\mathcal{L}_0 - in\omega_{\mathrm{in}})\,\rho_n + \mathcal{L}_1\rho_{n-1} + \mathcal{L}_{-1}\rho_{n+1} = 0\,, \tag{38}$$

and impose that $\rho_m = 0$ for a sufficiently large m.

The coherent emission intensity of the resonator at a frequency $n\omega_{\mathrm{in}}$ is proportional to $\mathrm{Tr}[X^+\rho_{-n}]$. For the transmission spectrum, where the coherent input $|\alpha_{\mathrm{in}}|/\sqrt{\omega_{\mathrm{in}}}$ at frequency ω_{in} is compared to the coherent output $\Phi^+_{\mathrm{r,out}}$ at the same frequency, we have

$$S_{21} = \sqrt{\frac{\omega_{\mathrm{in}}}{\omega_1}}\frac{\sqrt{\kappa_{\mathrm{r}}}}{|\alpha_{\mathrm{in}}|}\,\mathrm{Tr}\big[X^+\rho_{-1}\big]\,. \tag{39}$$

In the simple case of a single harmonic oscillator without internal loss ($\kappa_{\mathrm{int}} = 0$), we have

$$\mathrm{Tr}\big[X^+\rho_{-1}\big] = 2|\alpha_{\mathrm{in}}|\sqrt{\kappa_r}/(\kappa_r + \kappa_l) \tag{40}$$

on resonance, and the standard transmission formula is obtained [6]. For the SHG spectrum, we calculate the emission from the component oscillating at $2\omega_{\mathrm{in}}$. In other words,

$$S_{\mathrm{SHG}} \propto \mathrm{Tr}\big[X^+\rho_{-2}\big]\,. \tag{41}$$

In the case of the interference pattern in Fig. 4 of the main text, we used a drive with harmonics of frequency $\omega^{(1)}_{\mathrm{in}}$ and $\omega^{(2)}_{\mathrm{in}}$. In the first case, depicted in Fig. 4a,b of the main text, the interaction term $\mathcal{V}_{\mathrm{in}}$ on the left side becomes

$$\begin{aligned}\mathcal{V}_{\mathrm{in}}(t) = &2\sqrt{\kappa_l}\left[|\alpha^{(1)}_{\mathrm{in}}|\sqrt{\frac{\omega^{(1)}_{\mathrm{in}}}{\omega_1}}\sin\Big(\omega^{(1)}_{\mathrm{in}}t\Big)\right. \\ &\left. + |\alpha^{(2)}_{\mathrm{in}}|\sqrt{\frac{\omega^{(2)}_{\mathrm{in}}}{\omega_1}}\sin\Big(\omega^{(2)}_{\mathrm{in}}t + \phi\Big)\right]X\,,\end{aligned} \tag{42}$$

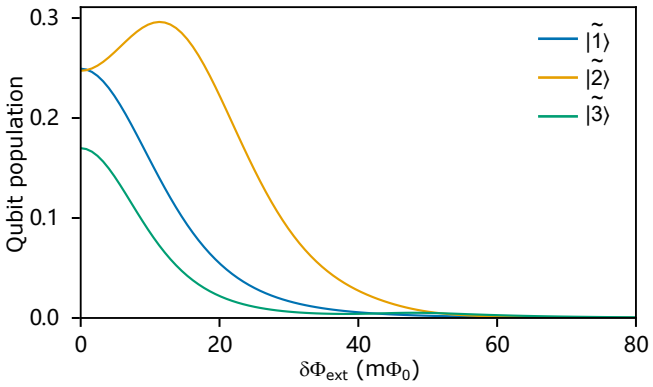

Supplementary Fig. 4. Population of the dressed qubit as a function of the flux bias $\delta\Phi_{\rm ext}$. The population is computed as $\langle\Sigma^-\Sigma^+\rangle$, with $\Sigma^+ = \sum_{j>k}\langle k|\sigma_z|j\rangle|k\rangle\langle j|$, and it is almost negligible in the region around $\delta\Phi_{\rm ext} \simeq 47\ {\rm m}\Phi_0$, demonstrating the pure-photonic nature of the effect.

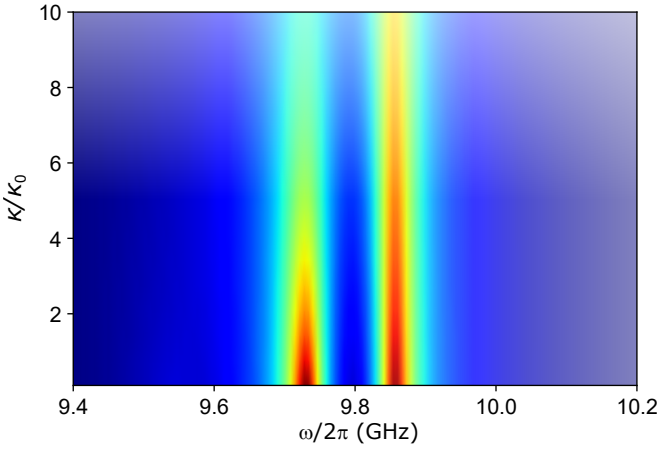

Supplementary Fig. 5. Rabi splitting visibility as a function of the qubit losses κ_q and $\kappa_{q,\rm dep}$ for both internal losses and pure dephasing. The value of the losses is normalized by the ones used in this work. As can be seen, aside from a small attenuation of the intensity, the Rabi splitting remains visible and distinguishable even at large qubit losses.

where ϕ is the relative phase between the two tones, and we vary the intensity of the second tone at frequency $\omega_{\rm in}^{(2)} = 2\omega_{\rm in}^{(1)}$. In the second case, as shown in Fig. 4c,d of the main text, we vary the intensity of the first tone, with the phase factor inside the first driving term rather than the second one. Since in the device presented here, the left port corresponds to the input port, while the right one is the output port, throughout this article we define $\kappa_{\rm in} \equiv \kappa_l$ and $\kappa_{\rm out} \equiv \kappa_r$ (see Supplementary Fig. 1). The estimation of the number of photons is performed following the standard formula of a simple driven-dissipative harmonic oscillator. Although in the USC regime, this might slightly change, it provides a simple formula relating the input power with the mean number of photons in the resonator and helps for comparison with standard quantum optics architectures. Thus, the mean number of photons in the first (second) mode is evaluated as

$$\bar{n}_1 = 4\frac{P_{\rm in}^1\kappa_{\rm in}}{\omega_1\Gamma_{1,0}^2}\,, \qquad \bar{n}_2 = 4\frac{P_{\rm in}^2\kappa_{\rm in}}{\omega_2\Gamma_{3,0}^2}\,. \tag{43}$$

Phase sensitivity of parametric amplification

The evolution equation for a linear degenerate parametric amplifier is (see, e.g., [8])

$$b = a\,{\rm cosh}r + e^{i\phi}a\,{\rm sinh}r\,, \tag{44}$$

where a and b are the input and output destruction photon operators at ω, r is a real constant determined by the strength and duration of the interaction (proportional to the pump amplitude at 2ω, and ϕ describes the pump phase. Assuming a coherent input at ω, $a \to \alpha$ with α real (corresponding to a relative phase between the two tones ϕ), in the weak r limit, we obtain

$$\langle b\rangle = \alpha(1 + e^{i\phi}r) \tag{45}$$

and thus

$$|\langle b\rangle|^2 = \alpha^2(1 + r\cos\phi)^2 + r^2\sin^2\phi\,, \tag{46}$$

showing an output signal at ω depending on both the phase and amplitude of the drive at 2ω, in qualitative agreement with the data shown in Fig. 4a in the main text.

Dependence of the Rabi splitting on the qubit decoherence rate

Here we demonstrate that, despite the non-negligible qubit decoherence in our device, the visibility of the effect (e.g., the Rabi splitting in Fig. 2 of the main text) is not significantly impacted by the qubit decoherence. Indeed, the qubit is very far detuned from the photonic resonance frequencies, especially in the region of the avoided-level-crossing. For this reason, as also shown in Supplementary Fig. 4, its participation in the dynamics is minimal. Supplementary Fig. 5 shows the photonic Rabi splitting as in Fig. 2 of the main text, as a function of the qubit losses κ_q and $\kappa_{q,\rm dep}$ for both internal losses and pure dephasing. The value of the losses is normalized by the ones used throughout the work. As already explained, the qubit participation is very small, and it does not affect the visibility, aside from a small attenuation. Indeed, we observe no significant linewidth broadening as the qubit losses increase. This fact is very important, because many qubits are susceptible to noise. Thus, this shows the robustness of our setup under nearly all conditions.

Photonic transition matrix elements

Many peculiar behaviors of the circuit-QED system investigated here can be understood based on a few photonic transition matrix elements, describing the strength

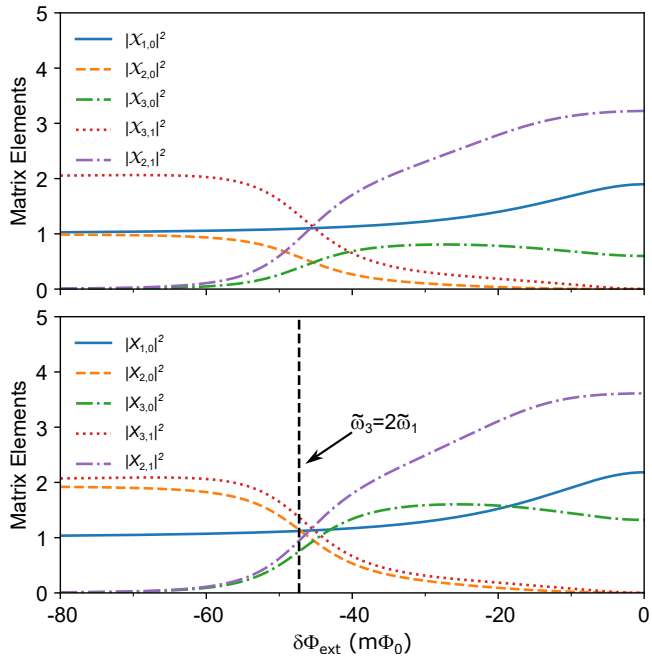

Supplementary Fig. 6. Relevant photonic transition matrix elements between the lowest energy levels of the system as a function of the flux offset. The matrix elements are calculated for both the input–output dissipation operator X (bottom panel) and $\mathcal{X}$ (upper panel).

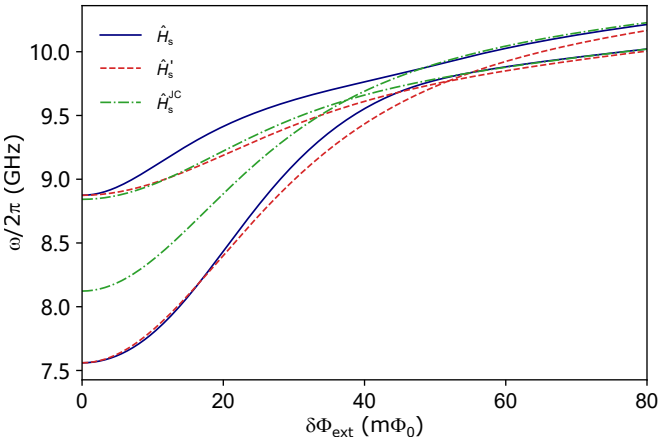

Supplementary Fig. 7. Energy levels in the region of the one-two-photon avoided level crossing obtained by diagonalizing three different Hamiltonians. The case with H_s is the only one showing the avoided level crossing, proving that both the counter-rotating terms and the parity symmetry breaking are needed to achieve this effect.

of transitions between the lowest energy levels of the system. We calculated them by direct numerical diagonalization of the Hamiltonian in Eq. (1) of the main text, after fixing parameters by fitting the experimental spectral lines in Fig. 2 of the main text.

Supplementary Fig. 6 shows the calculated off-diagonal matrix elements $\langle E_j|\mathcal{X}|E_k\rangle$ and $\langle E_j|X|E_k\rangle$, as a function of the flux offset, where $\mathcal{X} = a_1 + a_1^\dagger + a_2 + a_2^\dagger$ and X as in Supplementary Eq. (22). The eigenstates $|E_j\rangle$ of the Hamiltonian in Eq. (1) of the main text are sorted in ascending order so that $j > k$ for energy eigenvalues $\tilde{\omega}_j > \tilde{\omega}_k$. State $|E_1\rangle \equiv |\widetilde{1,0}\rangle \simeq |1,0,g\rangle$ corresponds to the dressed one-photon (of mode $n = 1$) state. The impact of the hybridization of one- and two-photon states around the avoided-level crossing ($\delta\Phi_{ext} \approx -47$ mΦ_0) is evident. For small absolute values of the flux offset $|\delta\Phi_{ext}|$, $|E_2\rangle \simeq |2,0,g\rangle$, and $|E_3\rangle \simeq |0,1,g\rangle$, while in the opposite limit, after the avoided-level crossing, ($|\delta\Phi_{ext}| > 80$ mΦ_0), $|E_2\rangle \simeq |0,1,g\rangle$, and $|E_3\rangle \simeq |2,0,g\rangle$. The vertical dashed line indicates the degeneracy condition where SHG occurs. Note that at this flux offset ($\delta\Phi_{ext} \sim -47$ mΦ_0) $|X_{1,0}|^2 \sim 1.2$, $|X_{3,1}|^2 \sim 1.4$, while $|X_{3,0}|^2 \sim 0.8$. The one–two-photon strong coupling gives rise to a harmonic three-level Δ system ($|E_0\rangle$, $|E_1\rangle$, $|E_3\rangle$), where $\tilde{\omega}_3 - \tilde{\omega}_1 = \tilde{\omega}_1 - \tilde{\omega}_0$, with all transition matrix elements comparable and close to the standard matrix element $\langle 0|a|1\rangle = 1$ for one-photon transition in vacuum. The matrix elements in Supplementary Fig. 6 enter in all the theoretical calculation displayed in this article and determine the observed nonlinear optical processes below the single-photon power level. Note that at $\delta\Phi_{ext} \sim -47$ mΦ_0 state $|E_3\rangle$ corresponds to the upper energy state $|\psi_+\rangle$ in the one–two-photon avoided level crossing, while $|E_2\rangle \equiv |\psi_-\rangle$ to the lower energy state.

Comparison with other Hamiltonians

It is useful to compare our model with other two cases. The first one without considering the parity symmetry breaking term, and the second one without including the counter-rotating terms. First, we express the original Hamiltonian in Eq. (1) of the main text using the basis where the qubit Hamiltonian is diagonal:

$$H_s = \frac{\omega_q}{2}\sigma_z + \sum_{n=1,2}\big[\omega_n a_n^\dagger a_n + g_n(a_n^\dagger + a_n)(-\sin(\theta)\sigma_x + \cos(\theta)\sigma_z)\big]\,. \tag{47}$$

Now, we can define the Hamiltonian H_s', obtained by neglecting the parity-symmetry breaking term in the interaction part:

$$H_s' = \frac{\omega_q}{2}\sigma_z + \sum_{n=1,2}\big[\omega_n a_n^\dagger a_n - \sin(\theta) g_n(a_n^\dagger + a_n)\sigma_x\big]\,, \tag{48}$$

and the Jaynes–Cummings equivalent Hamiltonian

$$H_s^{JC} = \frac{\omega_q}{2}\sigma_z + \sum_{n=1,2}\big[\omega_n a_n^\dagger a_n - \sin(\theta) g_n(a_n^\dagger \sigma_- + a_n\sigma_+)\big]\,. \tag{49}$$

Supplementary Fig. 7 shows the energy levels of these three Hamiltonians, proving that both the parity symmetry breaking and the counter-rotating terms are needed

to achieve the avoided-level crossing (and thus the strong coupling between one and two photons).

* litf@tsinghua.edu.cn
† salvatore.savasta@unime.it
‡ jqyou@zju.edu.cn

[1] J. Bourassa, F. Beaudoin, J. M. Gambetta and A. Blais, Josephson-junction-embedded transmission-line resonators: From Kerr medium to in-line transmon, Phys. Rev. A **86(1)**, 013814 (2012).

[2] B. Peropadre, D. Zueco, D. Porras, and J. J. García-Ripoll, Nonequilibrium and nonperturbative dynamics of ultrastrong coupling in open lines, Phys. Rev. lett. **111(24)**, 243602 (2013).

[3] A. Blais, A. L. Grimsmo, S. M. Girvin, and A. Wallraff, Circuit quantum electrodynamics, Rev. Mod. Phys. **93(2)**, 025005 (2021).

[4] J. Bourassa, J. M. Gambetta, A. A. Abdumalikov Jr, O. Astafiev, Y. Nakamura, and A. Blais, Ultrastrong coupling regime of cavity QED with phase-biased flux qubits, Phys. Rev. A **80(3)**, 032109 (2009).

[5] F. Yoshihara, T. Fuse, S. Ashhab, K. Kakuyanagi, S. Saito, and K. Semba, Superconducting qubit–oscillator circuit beyond the ultrastrong-coupling regime, Nat. Phys. **13(1)**, 44-47 (2017).

[6] D. F. Walls and G. J. Milburn, Quantum Optics, 2nd ed. (Springer, 2008).

[7] A. Settineri, V. Macrì, A. Ridolfo, O. Di Stefano, A. F. Kockum, F. Nori, and S. Savasta, Dissipation and thermal noise in hybrid quantum systems in the ultrastrong-coupling regime, Phys. Rev. A **98**, 053834 (2018).

[8] C. M. Caves, Quantum limits on noise in linear amplifiers, Phys. Rev. D **26**, 1817 (1982).